Detecting the Ratio of Rain and Cloud Water in Low-Latitude Shallow Marine Clouds

MATTHEW D. LEBSOCK, TRISTAN S. L'ECUYER, AND GRAEME L. STEPHENS

Colorado State University, Fort Collins, Colorado

(Manuscript received 16 February 2010, in final form 20 September 2010)

ABSTRACT

Satellite observations are used to deduce the relationship between cloud water and precipitation water for low-latitude shallow marine clouds. The specific sensors that facilitate the analysis are the collocated *CloudSat* profiling radar and the Moderate Resolution Imaging Spectroradiometer (MODIS). The separation of the cloud water and precipitation water signals relies on the relative insensitivity of MODIS to the presence of precipitation water in conjunction with estimates of the path-integrated attenuation of the *CloudSat* radar beam while explicitly accounting for the effect of precipitation water on the observed MODIS optical depth. Variations in the precipitation water path are shown to be associated with both the cloud water path and the cloud effective radius, suggesting both macrophysical and microphysical controls on the production of precipitation water. The method outlined here is used to place broad bounds on the mean relationship between the precipitation water path and the cloud water path in shallow marine clouds, given certain clearly stated assumptions. The ratio of precipitation water to cloud water is shown to increase from zero at low cloud water path values to roughly 0.5 at 500 g m^{-2} of cloud water. The retrieval results further show that the median influence of precipitation on the observed optical depth increases monotonically with optical depth varying between 1% and 5% at 500 g m^{-2} of cloud water with the source of the uncertainty deriving from the assumption of the nature of the precipitation drop size distribution.

1. Introduction

Recent observations have hinted at the ubiquitous nature of precipitation in shallow marine clouds (Haynes and Stephens 2007). Precipitation processes can affect cloud microphysics through the action of coalescence while they may also modulate cloud macrophysical structure (Paluch and Lenschow 1991; Comstock et al. 2005; Stevens et al. 1998) through the latent heating of condensation and evaporation. As is evidenced by the frequent occurrence of pockets of open cellular convection (Stevens et al. 2005; Wood et al. 2008) in drizzling stratocumulus, even modest precipitation rates can affect the mesoscale organization of warm clouds (Wang and Feingold 2009) and thus influence key macrophysical quantities such as cloud fraction and cloud liquid water path that govern the radiative effects of these clouds. The sensitive nature of the relationship between precipitation and low cloud cover contributes to uncertainty in anthropogenic modifications of the earth's climate. For example, the potential for pollution aerosol to suppress precipitation and alter cloud organization (Albrecht 1989) represents a large uncertainty in the understanding of anthropogenic forcing of the climate system. Furthermore, cloud feedbacks are widely understood as being the largest source of uncertainty in climate prediction (Stephens 2005; Dufresne and Bony 2008), and variability in the parameterization of warm clouds in climate models has been shown to dominate the total cloud feedback (Bony and Dufresne 2005; Webb et al. 2006). It is therefore critical that we improve our understanding of the relative frequency of occurrence and magnitude of precipitation in warm cloud regimes on the global scale.

Several remote sensing methods provide a window into the nature of global precipitation. The current generations of remote sensing techniques have difficulty quantifying precipitation from shallow weakly precipitating clouds, however. Passive estimates of precipitation are commonly provided by passive microwave techniques (Kummerow et al. 2001; Hilburn and Wentz 2008). In the case of shallow precipitation the algorithm must infer rain rates from an emission signal that is sensitive

Corresponding author address: Matthew D. Lebsock, Dept. of Atmospheric Science, 1371 Campus Delivery, Colorado State University, Fort Collins, CO 80523-1371.
E-mail: lebsock@atmos.colostate.edu

DOI: 10.1175/2010JAMC2494.1

to the presence of both cloud and precipitation water. These methods invariably suffer from an ambiguity regarding the ratio of cloud water emission to precipitation water emission and therefore must rely on assumptions from either cloud-resolving models (Kummerow et al. 2001) or climatological observations (Hilburn and Wentz 2008) to infer the cloud–rain partitioning. A recent algorithm (Haynes et al. 2009) applied to *CloudSat* radar data has demonstrated excellent ability in identifying weakly precipitating clouds. However, the attenuation-based precipitation algorithm must make analogous assumptions regarding the ratio of cloud to rainwater. An estimation-based retrieval utilizing both an attenuation constraint and the full radar reflectivity profile (L'Ecuyer and Stephens 2002; Mitrescu et al. 2010) may soon offer improved estimates of this partitioning from the *CloudSat* data. Note that the 13-GHz Tropical Rainfall Measuring Mission (TRMM) precipitation radar (PR; Iguchi et al. 2000) algorithm does not suffer from the ambiguity of an assumption regarding the cloud–rain partition because it is insensitive to small cloud droplets. Nonetheless, light precipitation may pass undetected by this sensor because reflectivity falls below the radar's minimum detectable signal of 17 dBZ because of low precipitation water contents, the presence of small drizzle droplets, partial beam filling of the radar volume, or some combination of the above. In fact, a recent analysis by Berg et al. (2010) estimates that the PR misses 59% of precipitation events and 9% of the total precipitation volume. Given the current ambiguous state of precipitation retrievals in shallow cloud regimes, there exists a need for the development of novel approaches of simultaneously inferring cloud and rainwater amounts.

Some progress toward the goal of inference of cloud-to-rainwater ratios has already occurred. For example, a series of papers (Masunaga et al. 2002a,b) uses multisensor information from the TRMM Microwave Imager (TMI) and Visible and Infrared Scanner (VIRS) sensors (Kummerow et al. 1998) to demonstrate the physical basis for a separation of the cloud and precipitation signals using both a solar scattering (VIRS) signal and an attenuation (TMI) signal. Shao and Liu (2004) utilize these same physical principles to establish a drizzle index that uses the TRMM observations. Rapp et al. (2009) demonstrate that TMI water path retrievals are improved when ancillary rain and cloud information from the PR and VIRS are included in the retrieval algorithm. Bennartz et al. (2010) infer the rainwater path of warm clouds from coincident observations from the Advanced Microwave Scanning Radiometer-Earth Observing System (AMSR-E) and the Spinning Enhanced Visible and Infrared Imager (SEVIRI). This study continues along this line of inquiry by introducing a multisensor technique to infer the column-integrated precipitation water path W_p as a function of the cloud water path W_c using two state-of-the-art sensors flying in the National Aeronautics and Space Administration (NASA) A-train constellation (Stephens et al. 2002; L'Ecuyer and Jiang 2010). Specifically, we employ retrieved optical depth τ and cloud effective radius $r_{e,c}$ based on visible and near-infrared reflectances from the Moderate Resolution Imaging Spectroradiometer (MODIS) instrument and the integrated two-way attenuation of the *CloudSat* Cloud Profiling Radar (CPR) beam. The method is premised on the assumption that visible and near-infrared observations are primarily sensitive to the presence of cloud while the CPR path-integrated attenuation $\mathrm{PIA}_{\mathrm{hydro}}$ is primarily sensitive to the presence of precipitation. The very different sensitivities of the optical and radar observations to cloud and precipitation water permit an estimate of the relative amounts of the cloud and precipitation water in the column.

2. Data

Three years (June 2006–May 2009) of collocated pixel-scale level-2 data from the *CloudSat* (Stephens et al. 2008) CPR, release 4 (R04), and MODIS MOD06 and MOD35 (Platnick et al. 2003) collection 5 are used in this study. The CPR and MODIS have similar fields of view, and therefore we assume that the two instruments are sampling approximately the same cloud volume. Both the MODIS cloud flags and the CPR-range-resolved reflectivity are used to reduce the data to shallow liquid clouds by following the method of Lebsock et al. (2008). In this study the data are further reduced to low-latitude clouds between 30°N and 30°S to avoid any potential biases in the MODIS cloud optical depth observations related to large solar zenith angles (Greenwald 2009). The pixel-resolution clouds that remain following the data screening have 10.8-μm brightness temperatures greater than 270 K, are identified as liquid by the MODIS microphysical retrieval, and have been screened for cirrus contamination using both the MODIS cirrus flag (Ackerman et al. 1998) and the *Cloud-Aerosol Lidar and Infrared Pathfinder Satellite Observation* (*CALIPSO*) lidar (Winker et al. 2007) cloud flags as implemented in the Geometric Profile (GEOPROF) lidar product. An attempt is made to minimize the effects of spatial heterogeneity on the MODIS retrievals by only retaining clouds that are identified by MODIS as 100% cloudy over a 5-km area surrounding the *CloudSat* pixel.

3. Method

a. Identification of cloud and precipitation

The precipitation flag in the *CloudSat* 2C Precipitation Column algorithm (2C-PRECIP-COLUMN) product (Haynes et al. 2009) is used to distinguish nonprecipitating scenes from those that are likely raining or drizzling. That product defines four rain categories (nonprecipitating, possible, likely, and certain) based on a combination of observed reflectivity and the two-way path-integrated attenuation (PIA) of the radar beam. In this study, these categories are condensed into two broad pixel classes (nonprecipitating and precipitating) in which the possible, likely, and certain pixels are all identified as precipitating. This new precipitating category exhibits attenuation-corrected near-surface reflectivity greater than −15 dBZ, which is indicative of the onset of drizzle (Frisch et al. 1995). As a result of condensing the precipitation flag, the precipitating category spans a large range of clouds from drizzling clouds in which precipitation is falling within a cloud but not reaching the ground to heavy rain. The nonprecipitating cases, on the other hand, are assumed to have negligible water in the precipitation mode.

We note that a −15-dBZ reflectivity can be reasonably explained by either large cloud droplets or the presence of drizzle. For example, using the formulas outlined in Matrosov et al. (2004), a reflectivity of −15 dBZ corresponds to a cloud droplet effective radius of 15.3 μm when a number concentration of 250 cm^{-3} is assumed and 23.3 μm when a number concentration of 20 cm^{-3} is assumed. For this reason we use the near-surface reflectivity as opposed to the maximum reflectivity to define the precipitation flag because one would not expect cloud droplets of this size to reside at cloud base.

b. Precipitation DSD

Throughout this paper, two different assumptions are made regarding the precipitation drop size distribution (DSD) to place broad bounds on the precipitation water–to–cloud water ratio. The precipitation DSD is generally assumed to follow a truncated exponential distribution $N(r)\,dr = N_o e^{-\lambda r}\,dr$, where the truncation occurs at 30 μm. The first is a Marshall–Palmer distribution (Marshall and Palmer 1948) in which variations in rainwater content are determined entirely by modulation of the slope parameter λ, which imposes a positive correlation equal to 1 between the droplet number concentration and the mean radius of the distribution. The second distribution is a drizzle distribution qualitatively based on the results of Comstock et al. (2004), who found that variations in the precipitation water content are dominated by variations in the drizzle drop number concentration, with a nonnegligible influence from variations in the mean droplet radius, and that the variability in these parameters is negatively correlated. Loosely based on these observations, the drizzle distribution is described by the expression $\lambda = [20 \log_{10}(l_p + 4) + 30]^{-1}$, where l_p is the precipitation water content in grams per meter cubed, λ is in units of inverse micrometers, and N_o varies with λ to match l_p. This relationship imposes the observed negative correlation between droplet number concentration and mean radius below mean radii values of 52 μm and reverses the sign of the correlation above this threshold, allowing the distribution to take on a salient feature of the Marshall–Palmer distribution as water content increases.

c. Water path estimates

1) MODIS CLOUD WATER PATH

If it is assumed that the MODIS observations are insensitive to the presence of precipitation, estimates of W_c are provided from the cloud optical depth τ_c and cloud effective radius $r_{e,c}$ products by

$$W_c = \gamma_c \rho_w \tau_c r_{e,c}, \tag{1}$$

where γ_c is a scaling parameter related to the vertical distribution of water and the interpretation of the retrieved $r_{e,c}$. Assuming a vertically homogenous cloud gives $\gamma_c = 2/3$ (Stephens 1978), where $r_{e,c}$ is interpreted as a water content–weighted mean radius. If one assumes a nonprecipitating adiabatic cloud in which cloud water content increases linearly with height, it is straightforward to show (Szczodrak et al. 2001; Bennartz 2007) that $\gamma_c = 5/9$, where $r_{e,c}$ is interpreted as the cloud-top effective radius. To some extent the second expression is more appealing because it includes an additional level of realism without adding to the complexity of the calculation. There is observational evidence of the approximate adiabaticity of stratocumulus clouds (Albrecht et al. 1990; Brenguier et al. 2003; Wood 2005a); however, geometrically thicker shallow cumulus clouds display water contents much lower than those predicted by adiabatic theory (Warner 1970; Rauber et al. 2007).

Related to the interpretation of the observed effective radius is the complication that $r_{e,c}$ may be derived from any nonconservative scattering near-infrared wavelength. In the particular case of MODIS, three estimates of $r_{e,c}$ are made using the 1.6-, 2.1-, and 3.7-μm channels, each of which has a different penetration depth corresponding to different levels in the cloud (Platnick 2000). For example, radiation at 3.7 μm is absorbed more strongly by water drops than at the other wavelengths,

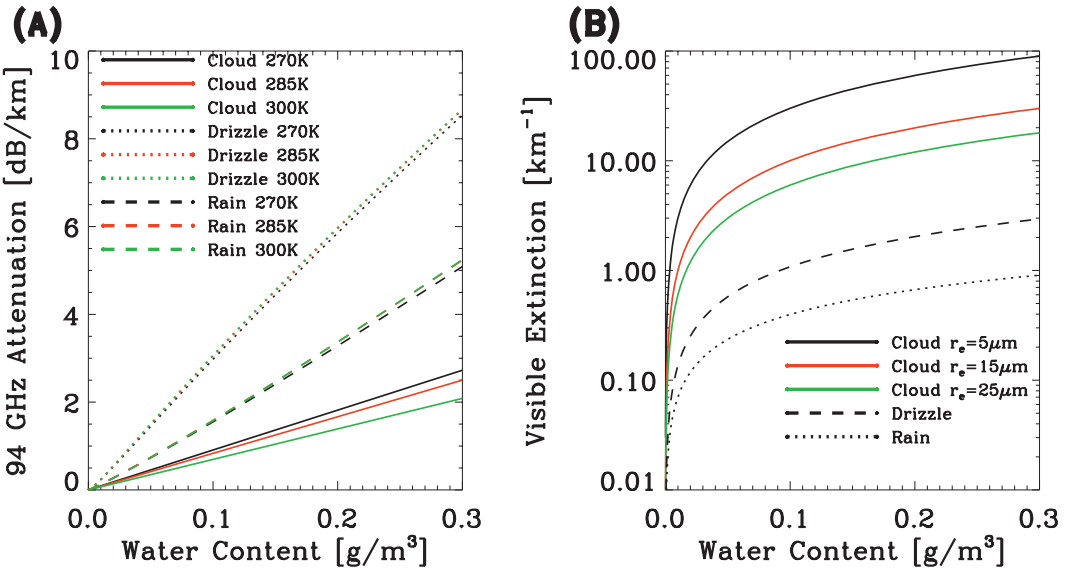

FIG. 1. (a) The attenuation at 94 GHz as a function of water content for various temperatures and DSDs. (b) The visible volume extinction coefficient for various hydrometeor distributions, with the assumption that the extinction efficiency is equal to 2. The 94-GHz cloud attenuation is modeled by the Rayleigh approximation under which attenuation is solely governed by water content. Details of the precipitation DSDs are provided in the text.

causing it to have the greatest sensitivity to the cloud-top radius. Because large precipitation-size drops tend to reside below cloud top, it is reasonable to assume that $r_{e,c}$ derived from the 3.7-μm channel will be less sensitive to the presence of precipitation than will the other channels. This is a common assumption that has some theoretical underpinning (Chang and Li 2002; Nakajima et al. 2010) and will be further justified by the results of this study.

2) *CloudSat* water path and attenuation

The PIA is defined as the two-way attenuation of the radar beam due to gases and hydrometeors. In decibel units this may be expressed as

$$\mathrm{PIA} = \mathrm{PIA}_{\mathrm{gas}} + \mathrm{PIA}_{\mathrm{hydro}} = 2\int_0^{\infty} (k_{\mathrm{gas}} + k_{\mathrm{hydro}})\, dz, \quad (2)$$

where k is the volume extinction coefficient. $\mathrm{PIA}_{\mathrm{gas}}$ may be calculated from model temperature and moisture fields, allowing $\mathrm{PIA}_{\mathrm{hydro}}$ to be found as the difference between $\mathrm{PIA}_{\mathrm{gas}}$ and the observed PIA. $\mathrm{PIA}_{\mathrm{hydro}}$ may further be divided into cloud and precipitation components:

$$\mathrm{PIA}_{\mathrm{hydro}} = \mathrm{PIA}_{\mathrm{cloud}} + \mathrm{PIA}_{\mathrm{precip}}. \quad (3)$$

At the CPR frequency of 94 GHz, attenuation due to cloud water is modeled well by the Rayleigh approximation. In this case the cloud water path W_c is linearly related to the vertically integrated attenuation, where the magnitude of the relationship between W_c and $\mathrm{PIA}_{\mathrm{cloud}}$ has a modest dependence on temperature T. The Rayleigh approximation breaks down at 94 GHz for precipitation-sized drops, and attenuation must be modeled using Mie theory, which introduces a dependence on the precipitation DSD. By treating the cloud and precipitation modes separately, the total water path may be expressed as

$$W_T = W_c + W_p = \alpha_c(T)\mathrm{PIA}_{\mathrm{cloud}} + \alpha_p(T, \mathrm{DSD})\mathrm{PIA}_{\mathrm{precip}}, \quad (4)$$

where $\alpha_{c,p}$ is an attenuation coefficient relating the PIA to the cloud or precipitation water path. Figure 1a shows α for various combinations of temperature and DSD. Note the modest temperature dependence of α for cloud water and the strong dependence on the details of the DSD for precipitation water. Further details describing the temperature and DSD dependence of the attenuation of millimeter-wave radar are described in Lhermitte (1990).

3) Combining MODIS and *CloudSat*

The previous two sections describe the theoretical foundation for simultaneous derivation of the cloud and precipitation water path from the combination of MODIS and *CloudSat* observations. This section formalizes the approach given certain assumptions. To begin, if one were to assume that the optical measurements were insensitive to the presence of precipitation, then the cloud

water path would derive entirely from the MODIS observations [Eq. (1)],

$$W_c = \gamma_c \tau r_{e,c}, \tag{5}$$

and the precipitation water path would then follow from the *CloudSat* PIA estimate [Eqs. (3) and (4)],

$$W_p = \alpha_p(\mathrm{PIA} - W_c/\alpha_c). \tag{6}$$

Figure 1b shows that in general the extinction by cloud droplets is an order of magnitude larger than that of precipitation drops for a given liquid water content. Nonetheless, here we relax the above restriction by assuming that the MODIS effective radius observation is insensitive to the presence of precipitation because of the limited penetration depths of the near-infrared channels but that the optical depth, which is a cloud-integrated parameter, is sensitive to the presence of precipitation. In this case the optical depth can be written as the sum of the cloud and precipitation component,

$$\tau = \tau_c + \tau_p, \tag{7}$$

and it follows that

$$\tau = \kappa_c W_c + \kappa_p W_p, \tag{8}$$

where $\kappa_c = (\rho\gamma_c r_{e,c})^{-1}$ and $\kappa_p = (\rho\gamma_p r_{e,p})^{-1}$. Here, $r_{e,p}$ is a function of the precipitation DSD and γ_p is set equal to the familiar value of $^2/_3$ whereas $r_{e,c}$ and γ_c are derived from the MODIS observations.

With the assumption of a precipitation DSD and the insensitivity of the MODIS effective radius to the presence of precipitation, Eqs. (1), (3), (4), (7), and (8) represent a closed system of equations for W_c and W_p given observations of τ and PIA. The solution to these equations follows from algebraic manipulation as

$$W_c = \frac{\alpha_p \mathrm{PIA} - \tau/\kappa_p}{(\alpha_p/\alpha_c) - (\kappa_c/\kappa_p)} \quad \text{and} \tag{9}$$

$$W_p = \frac{\alpha_c \mathrm{PIA} - \tau/\kappa_c}{(\alpha_c/\alpha_p) - (\kappa_p/\kappa_c)}. \tag{10}$$

To understand these equations better, it is instructive to examine the limiting case in which the precipitation optical depth is assumed to be 0 and thus $\kappa_p = 0$. In this case the equations revert to the simpler expressions given by Eqs. (5) and (6), where the cloud water is derived entirely from the MODIS observations and the precipitation water follows from the PIA minus a correction due to the MODIS cloud water. It can be seen then that Eqs. (9) and (10) represent more general forms of Eqs. (5) and (6) with the additional coupling between the two equations given by κ_p, which describes the magnitude of the influence of precipitation water on the observed optical depth. Through the use of Eqs. (9) and (10), the results that follow show that the influence of precipitation mode water on the cloud optical depth is generally less than 10% and in the median lies between 1% and 5%, depending on the assumed shape of the DSD.

In practice, Eqs. (9) and (10) must be solved iteratively because of the dependence of the precipitation attenuation coefficients α_p and κ_p on the precipitation liquid water content. An initial guess is made of the liquid water content and associated values of α_p and κ_p. The values of W_c and W_p are then calculated. The precipitation water content is then recalculated by assuming that the precipitation is uniformly distributed throughout the column and that the radar determines the top of the rain column. The attenuation coefficients are adjusted accordingly, and the calculation is repeated until a convergent answer is reached, which typically takes three or fewer iterations.

Calculation of the attenuation coefficients $\alpha_c(T)$, $\alpha_p(T, \mathrm{DSD})$, and $\kappa_p(\mathrm{DSD})$ requires ancillary information regarding the atmospheric temperature structure and the precipitation DSD. We account for the temperature variation using a cloud mean temperature derived from the reflectivity profiles in the *CloudSat* 2B-GEOPROF product and the temperature profiles in the European Centre for Medium-Range Weather Forecasts (ECMWF) auxiliary analysis (ECMWF-AUX) product. In the specific case of nonprecipitating clouds, no DSD assumption is necessary and there is a unique relationship between W_c and $\mathrm{PIA}_{\mathrm{hydro}}$. *CloudSat* and MODIS will therefore provide two independent estimates of W_c for nonprecipitating clouds. In the case of precipitating clouds, we must assume a DSD, introducing an element of uncertainty that can at best be estimated by varying the assumed DSD.

We must mention that an additional source of uncertainty derives from potential contamination of the surface return due to multiple scattering (Battaglia and Simmer 2008). Multiple scattering would tend to negatively bias the PIA estimate and thus the W_T; however, the influence of multiple scattering in these shallow low-water-path clouds is expected to be negligible (Battaglia et al. 2008) in comparison with the other uncertainties.

d. PIA estimates

Haynes et al. (2009) outline a method for estimating $\mathrm{PIA}_{\mathrm{hydro}}$ over the global oceans using a climatological database of the clear-sky surface cross section ($\sigma_{o,\mathrm{clr}}$) for

various wind speeds U and sea surface temperatures (SST). $\mathrm{PIA}_{\mathrm{hydro}}$ may be calculated from the observed surface cross section σ_o for cloudy-sky scenes as $\mathrm{PIA}_{\mathrm{hydro}} = \sigma_{o,\mathrm{clr}}(U, \mathrm{SST}) - \sigma_o - \mathrm{PIA}_{\mathrm{gas}}$. $\mathrm{PIA}_{\mathrm{gas}}$ is estimated from temperature and humidity fields in the *CloudSat* ECMWF-AUX product. Following the uncertainty analyses of Eyre (1990) and Eyre et al. (1993), the uncertainty in the model humidity fields is approximately 15%. $\mathrm{PIA}_{\mathrm{gas}}$ is linear with column water vapor to a very good approximation, meaning that the $\mathrm{PIA}_{\mathrm{gas}}$ estimate will also be uncertain by 15%. For the pixels retained in this analysis, this leads to a mean uncertainty in $\mathrm{PIA}_{\mathrm{gas}}$ of 0.52 dB. Haynes et al. (2009) also adopt wind speed and SST from the ECMWF model analysis because of potential contamination of the passive microwave observations in the presence of precipitation.

Here, we introduce an independent estimate of $\mathrm{PIA}_{\mathrm{hydro}}$ that we believe to be more accurate than the database method. The method employs an along-track interpolation of the clear-sky surface cross section into cloudy pixels. The primary advantage of this method is that it does not depend on the ECMWF model-derived fields so that uncertainty in the model-derived moisture and humidity fields is minimized. The details of the method are outlined below:

1) 100 pixels surrounding each cloudy pixel (as identified in the *CloudSat* 2B-GEOPROF-lidar product) are isolated.
2) The 10 closest observations of $\sigma_{o,\mathrm{clr}}$ on either side of the cloudy pixel are put into a subset, along with their pixel position. Linear regression is performed between pixel position and $\sigma_{o,\mathrm{clr}}$. If 20 clear-sky pixels are not available, then no estimate of $\mathrm{PIA}_{\mathrm{hydro}}$ is made.
3) The linear fit is used to estimate $\sigma_{o,\mathrm{clr}}$ for the cloudy pixel, and $\mathrm{PIA}_{\mathrm{hydro}}$ is then calculated as $\hat{\sigma}_{o,\mathrm{clr}} - \sigma_o$, where the caret denotes an estimate based on the linear interpolation. Uncertainty in the PIA is calculated as $\delta_{\mathrm{PIA}} = (\delta^2_{\sigma_o} + \delta^2_{\hat{\sigma}_{o,\mathrm{clr}}})^{1/2}$.

The drawback of this method is that it requires observations of $\sigma_{o,\mathrm{clr}}$ near cloudy pixels and cannot be used in substantially overcast scenes. In the analysis that follows, only pixels in which the mean distance between the clear-sky pixels used to create the linear fit and the cloudy pixel in question is less than 37 km (30 pixels) are retained. For this subset, the uncertainty is dominated by the uncertainty in the observed surface cross section δ_{σ_o}, which has a constant value of 1 dB, as opposed to uncertainty in the linear fit $\delta_{\hat{\sigma}_{o,\mathrm{clr}}}$, which has a mean value of 0.24 dB.

Figure 2 shows a joint histogram of the two estimates of $\mathrm{PIA}_{\mathrm{hydro}}$. Two notable features are immediately evident.

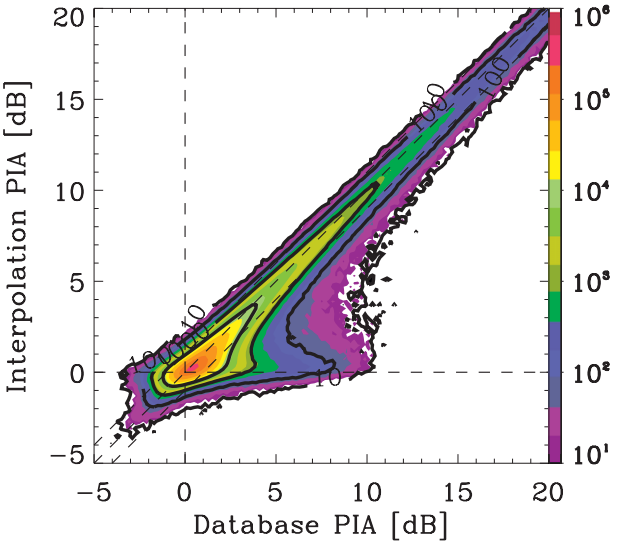

FIG. 2. Joint distribution of the climatological database and along-track interpolation estimates of the PIA. The three diagonal dashed lines correspond to the 1-to-1 line and the ±1-dB uncertainty estimate. The vertical and horizontal dashed lines show the zero coordinate axes.

First, a nearly constant 0.5-dB bias is observed in the database estimate relative to the interpolation estimate of $\mathrm{PIA}_{\mathrm{hydro}}$. We speculate that this bias may result from subgrid-scale variability in the ECMWF model humidity and wind speed fields that are largely accounted for in the interpolation method. In particular, small-scale variations in winds in the immediate vicinity of precipitation that are not captured by the model with its native resolution of 0.5° should be represented in the interpolation method. Second, a spur of the joint histogram occurs in which the database estimate substantially overestimates the interpolation method at low values of $\mathrm{PIA}_{\mathrm{hydro}}$. Isolating the data composing this spur shows that nearly all of these cases are those in which the surface wind speed is less than 4 m s^{-1} (not shown). Uncertainty in the database estimates of $\sigma_{o,\mathrm{clr}}$ approaches 20 dB under these low–wind speed conditions because of the rapid increase of $\sigma_{o,\mathrm{clr}}$ with decreasing wind speed from 0 to 4 m s^{-1}. Furthermore, the nonlinear nature of the relationship between U and $\sigma_{o,\mathrm{clr}}$ (Haynes et al. 2009) would lead us to suspect the positive bias (as opposed to random uncertainty) seen in Fig. 2 in these particular low–wind speed situations.

Figure 2 suggests that the database estimate of $\mathrm{PIA}_{\mathrm{hydro}}$ is unreliable at wind speeds below 4 m s^{-1}. However, if the low–wind speed cases are eliminated, a 0.5-dB bias is still evident in the remaining database estimates of $\mathrm{PIA}_{\mathrm{hydro}}$. This is not a major issue in the case of a heavily precipitating cloud in which the attenuation due to precipitation far surpasses that of cloud. A 0.5-dB bias is

approximately equivalent to the attenuation of a cloud with a water path of 60 g m^{-2}, however, which is a fairly typical value for stratocumulus cloud regimes. For the purposes of this study, we wish to be able to observe attenuation by nonprecipitating clouds, and therefore we restrict the analysis to cases in which the interpolation-based estimate is available. This is a conservative decision designed to maximize the accuracy of the PIA estimate, which limits the data to 2.1% of the total shallow-cloud data available, providing 73 100 unique pixels. This number is artificially low as a result of a known error in the GEOPROF lidar product (R04) that causes an overestimation of boundary layer cloudiness and will be corrected in the R05 release. Even after the correction to the GEOPROF lidar algorithm, future work must focus on correcting the bias identified in the climatological database estimates of the PIA to expand the feasibility of the method developed here to heavily overcast scenes.

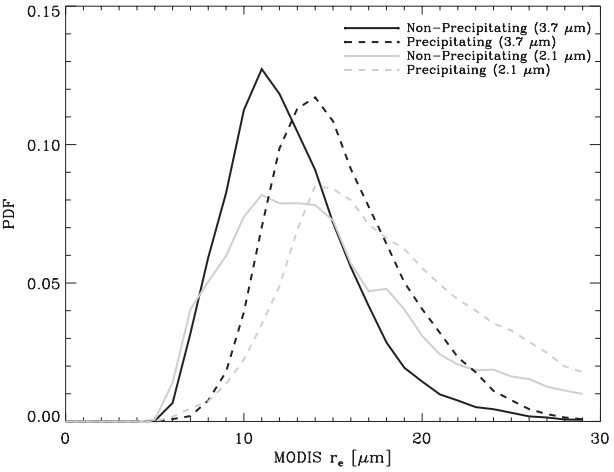

FIG. 3. PDFs of the MODIS effective radius r_e estimates for the 3.7- and 2.1-μm channels. Note the extension of the 2.1-μm distribution beyond 30 μm for both precipitating and nonprecipitating clouds. Statistics of the distributions are provided in Table 1.

4. Results and discussion

a. Effective radius

In the previous section it was speculated that the effective radius derived from the 3.7-μm channel would be more representative of the cloud-top radius and thus less sensitive to the presence of precipitation than the 2.1- or 1.6-μm channels because of its shallow penetration depth. Evidence suggestive of this tendency is presented in Fig. 3 and Table 1, which show the distribution of r_e retrieved from the 3.7- and 2.1-μm channels (results for 1.6 μm are nearly identical to those for 2.1 μm). The distribution of $r_{e,3.7}$ has a smaller mean value and tends toward 0 for radii in excess of 30 μm, whereas $r_{e,2.1}$ shows a tail that extends to radii larger than the 30-μm threshold beyond which MODIS does not provide effective radii estimates. This result may be indicative of the sensitivity of the 2.1-μm channel to large precipitation-size drops residing deeper in clouds, suggesting that the 3.7-μm channel may offer the W_c estimate that is least influenced by precipitation. These tendencies are evident even for clouds that are categorized as nonprecipitating, which may imply a ubiquitous presence of small numbers of large droplets affecting the 1.6- and 2.1-μm channels or may reflect a nonadiabatic cloud profile in which droplet size decreases with height near cloud top.

With knowledge of the penetration depths of the 3.7- and 2.1-μm channels, the adiabatic model predicts that $r_{e,3.7}$ is greater than $r_{e,2.1}$ for nonprecipitating clouds. Figure 3 and the statistics in Table 1 demonstrate that the observations show the opposite behavior. These observational results suggest that the sign of the difference between $r_{e,3.7}$ and $r_{e,2.1}$ may be sensitive to cloud-top entrainment effects as well as the presence of drizzle within cloud, which is consistent with the sensitivity analysis presented by Nakajima et al. (2010). To explore these points further, Fig. 4 shows the joint distribution of $r_{e,2.1}$ and $r_{e,3.7}$. This figure shows a very modest average tendency for adiabadicity ($r_{e,3.7} > r_{e,2.1}$) when $r_{e,2.1}$ is less than 10 μm. Beyond this point, $r_{e,2.1}$ begins to overestimate $r_{e,3.7}$, which is suggestive of the onset of coalescence processes.

In addition to the inference that $r_{e,3.7}$ provides the best estimate of the cloud-top radius, several additional important points may be made regarding Figs. 3 and 4. First, it is worth noting the large overlap between the precipitating and nonprecipitating r_e distributions that suggests that use of r_e alone to identify precipitation is entirely inappropriate. This observation fits well with parameterizations of the autoconversion process that depend more strongly on the cloud water content than on the cloud droplet number concentration (Wood 2005b). Second, the sign of the difference between $r_{e,3.7}$ and $r_{e,2.1}$ has a complicated dependency on $r_{e,2.1}$ and is

TABLE 1. Statistics for the effective radii distributions shown in Fig. 3.

	Nonprecipitating		Precipitating	
Channel (μm):	2.1	3.7	2.1	3.7
Mean ± std dev (μm)	15.2 ± 5.3	13.2 ± 3.6	18.3 ± 5.0	15.8 ± 3.7
Median (μm)	14.3	12.7	17.7	15.3

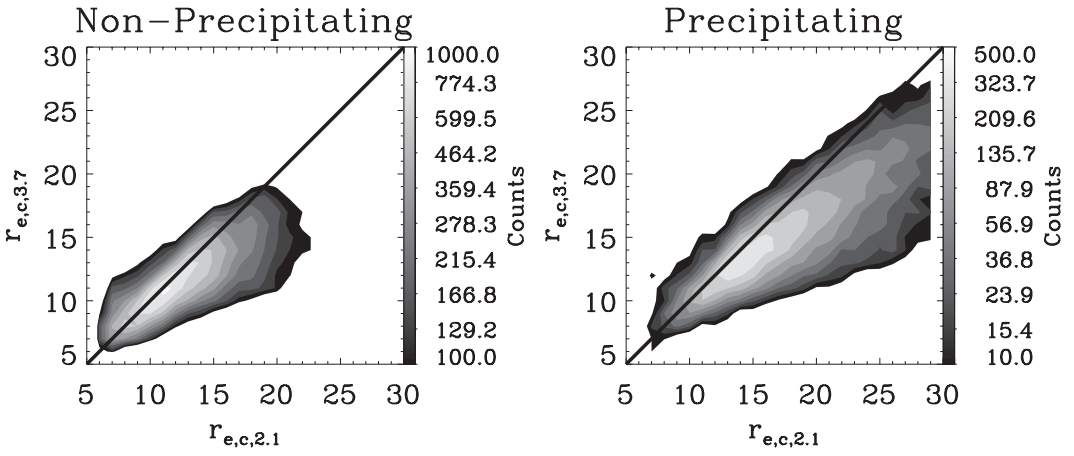

FIG. 4. Joint PDFs of the MODIS r_e estimates for the 3.7- and 2.1-μm channels. Below $r_{e,2.1}$ of 10 μm, the two estimates agree well, with the 3.7-μm channel slightly overestimating the 2.1-μm channel. Above this threshold, $r_{e,2.1}$ overestimates $r_{e,3.7}$ by increasing amounts.

not by itself a useful indicator of the presence of precipitation. A more appropriate precipitation index should most likely be based on several parameters including $r_{e,3.7}$, $r_{e,3.7} - r_{e,2.1}$, and τ. Third, from an algorithmic point of view, the results further suggest that the arbitrary truncation of the reported MODIS r_e at 30 μm may result in the loss of some information, particularly at the 2.1- and 1.6-μm channels where there is a tendency to retrieve values larger than 30 μm.

b. Nonprecipitating cloud water path

Figure 4 shows the *CloudSat* attenuation-based W_c plotted against the MODIS W_c derived from using the 3.7-μm channel and $\gamma_c = 5/9$ for all nonprecipitating pixels using Eq. (1). As previously mentioned, in this special case of nonprecipitating clouds, α is merely a function of temperature, which is taken from the ECMWF-AUX product, and the details of the cloud droplet size distribution are unimportant. Because these clouds are nonprecipitating, W_T is equivalent to W_c so that *CloudSat* provides an independent estimate of the same quantity using Eq. (4). A large amount of scatter is evident in the *CloudSat* data, which is consistent with the uncertainty in the PIA estimate of approximately 1 dB ($\sim$120 g m^{-2}). Important, however, is that negligible bias is observed between the two estimates of W_c along the entire range of data.

Table 2 provides summary statistics for the linear regression of *CloudSat* W_c onto the various MODIS cloud water paths. Note that the correlation coefficients for these fits are approximately 0.5, resulting from the imprecise nature of the *CloudSat* observations. However, it is expected that the *CloudSat* observations, which depend only on temperature, will be more accurate than the various MODIS observations, which depend on the assumed value of γ_c. We therefore use the *CloudSat* observations to determine the most appropriate estimate of $r_{e,c}$ and associated value of γ_c for the derivation of cloud water path from this dataset. Cloud water path derived from the 3.7-μm channel offers the least biased result, consistent with the assumption that this channel is most representative of the droplet radius at cloud top. This result is in agreement with the recent work of Greenwald (2009), who found that the adiabatic approximation yields improved agreement between the MODIS and Advanced Microwave Scanning Radiometer for Earth Observing System (AMSR-E) W_c values. The minimal bias between W_c derived from *CloudSat* and W_c derived using 3.7 μm bolsters confidence in both estimates as accurate measures of the cloud water path, although it must be reiterated that the agreement

TABLE 2. Summary statistics for the linear regression of *CloudSat* cloud water path onto six different estimates of the MODIS cloud water path for nonprecipitating clouds. Note that the slope found using the MODIS 3.7-μm channel and the adiabatic stratification (slope = 0.98) minimizes the bias between the two estimates. The sample size is N = 68 433. The *CloudSat* and MODIS data both display serial autocorrelation, leading to an effective sample size N^* = 26 853, where N^* is calculated using the formula $N^* = N(1 - r_1r_2)/(1 + r_1r_2)$, where r_1 and r_2 are the lag-1 autocorrelations of the two datasets (Bretherton et al. 1999). A one-sided Student's t test gives the statistical significance of the correlations at greater than the 99% level.

	Adiabatic ($\gamma_c = 5/9$)			Homogenous ($\gamma_c = 2/3$)		
Channel (μm):	3.7	2.1	1.6	3.7	2.1	1.6
Intercept	3.36	2.19	9.61	3.36	2.19	9.61
Slope	0.98	0.93	0.75	0.82	0.77	0.62
Correlation	0.49	0.50	0.47	0.49	0.50	0.47

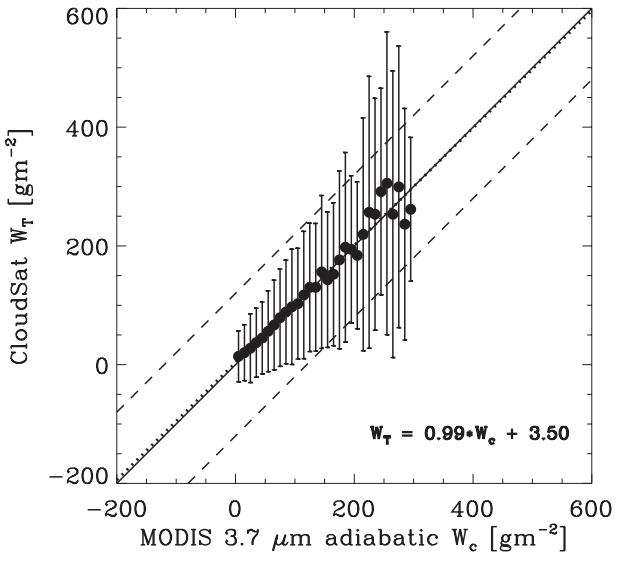

FIG. 5. The *CloudSat* attenuation-based cloud water path estimate W_T as a function of the MODIS 3.7-μm estimate W_c using the adiabatic assumption for nonprecipitating pixels. The circles and error bars show the mean and the standard deviation. The solid line shows the 1-to-1 line, and the dashed lines show the $\pm$120 g m^{-2} ($\sim$1 dB) bounds. The dotted line shows the linear best fit. Note the negligible bias between the two estimates.

between the two estimates is only valid in a statistical sense because of the large amount of scatter in the *CloudSat* PIA values.

Based on the results shown in Fig. 5 and Table 2 as well as on the $r_{e,c}$ distributions shown in Figs. 3 and 4, the remainder of this paper will refer to W_c as that derived using the 3.7-μm channel and $\gamma_c = 5/9$. Although not the central focus of this work, we pause here to note that the agreement between the PIA and W_c derived using $r_{e,3.7}$ and the adiabatic approximation does not necessarily verify the adiabatic model and that the agreement between the two cloud water estimates may be merely coincidental.

c. *Estimating the relationship between cloud water and precipitation water*

Using the statistical agreement between *CloudSat* and MODIS water path estimates in nonprecipitating clouds as a foundation, it is possible to exploit these instruments to separate the cloud and rain contributions to total water path in precipitating scenes. Equations (9) and (10) are solved to produce simultaneous estimates of W_c and W_p. Results are shown in Fig. 6 for all pixels as well as the subset of precipitating pixels. For reference, these figures also show lines of constant ratio (W_p:W_c). A trend of increasing W_p with increasing W_c is seen, with precipitation-to-cloud ratio increasing from approximately 0 at $W_c = 0$ g m^{-2} to approximately 0.5 at $W_c =$ 500 g m^{-2}. This behavior is consistent with in situ observations that show a correlation between precipitation and W_c (Pawlowska and Brenguier 2003; Comstock et al. 2004; vanZanten and Stevens 2005). An interesting feature observed in Fig. 6 is the occurrence of nonzero W_p at very low values of W_c in the precipitating subset. These pixels may be indicative of rainout processes, in which

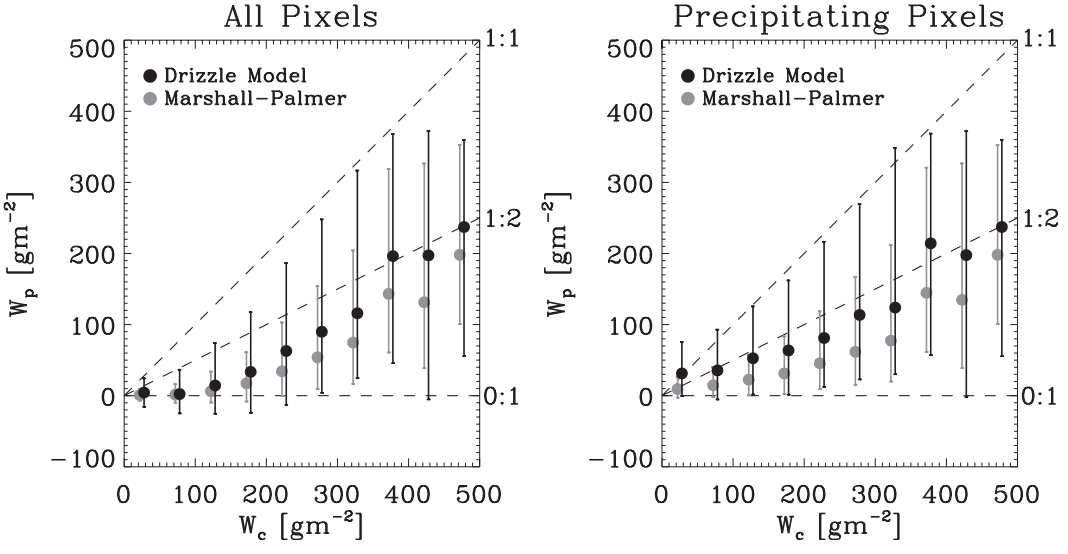

FIG. 6. Estimates of the mean relationship between the cloud water path W_c and the precipitation water path W_p given two assumptions regarding the precipitation DSD. The parameters that describe the DSD are described in the text. The circles and error bars respectively show the median value and the range of 75% of the data. The dashed lines show the ratio W_p:W_c for values of 1:1, 1:2, and 0:1, as indicated on the right axis.

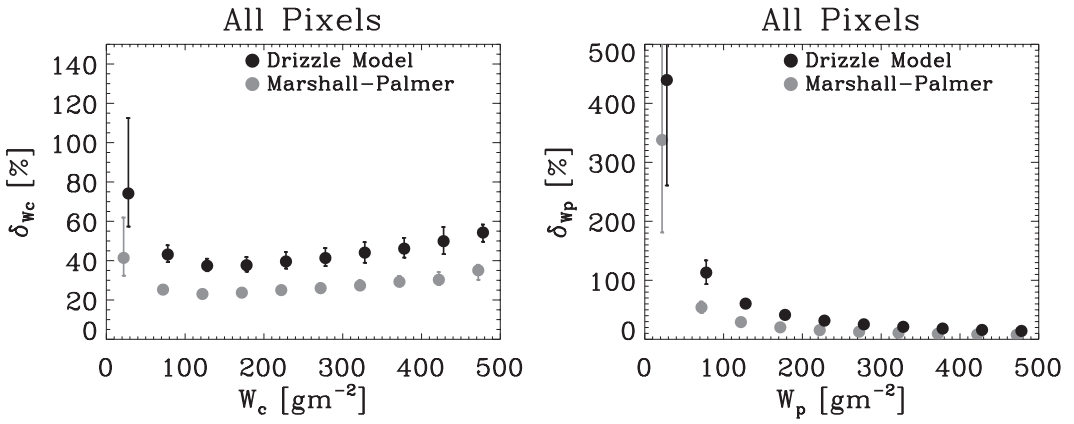

FIG. 7. The median percent uncertainty δ of the (left) cloud and (right) precipitation water paths. The error bars show the range encompassing 75% of the data.

residual precipitation remains but cloud water has been depleted. Note that this feature is not evident in the all-pixels plot, which is dominated by nonprecipitating clouds at water paths below about 150 g m^{-2} and precipitating clouds above approximately 300 g m^{-2}.

Uncertainties in the retrieved values of W_c and W_p are estimated using standard error propagation techniques as

$$\delta_W = \left[\left(\frac{\partial W}{\partial \mathrm{PIA}} \right)^2 \delta_{\mathrm{PIA}}^2 + \left(\frac{\partial W}{\partial \tau} \right)^2 \delta_\tau^2 + \left(\frac{\partial W}{\partial r_e} \right)^2 \delta_{r_e}^2 + 2 \frac{\partial W}{\partial \tau} \frac{\partial W}{\partial r_e} \delta_{\tau r_e} \right]^{1/2}, \quad (11)$$

where the MODIS cloud product provides $\delta\tau$ and δr_e and $\delta\tau r_e$ represents the covariance of the MODIS optical depth and effective radius uncertainties, which are highly correlated. The value of δ_{PIA} is derived as outlined in section 3d. Figure 7 highlights the behavior of the uncertainties, which are strong functions of the retrieval state space. From Fig. 7 the uncertainty in W_c can be roughly approximated as 50% whereas the uncertainty in W_p decreases from greater than 100% at values of less than 100 g m^{-2} to less than 20% at values of several hundred grams per meter squared. From these uncertainty estimates, we can conclude that much of the variability apparent in Fig. 6 is derived not from natural sources but rather from the imprecision inherent in the satellite observations.

Figure 8 shows the mean W_p as a function of W_c for various values of $r_{e,c,3.7}$. This figure highlights a clear association between cloud droplet size and W_p. This observation provides evidence for a frequently speculated pathway (Albrecht 1989) whereby anthropogenic cloud condensation nuclei could influence the precipitation water content and thus the rain rate of shallow maritime clouds through modification of the droplet size distribution and thus the coalescence rate. The dependence of W_p on both the cloud water path and the effective radius shown in Fig. 8 is consistent with previous analyses (Lebsock et al. 2008; Leon et al. 2008; Kubar et al. 2009; L'Ecuyer et al. 2009) of *CloudSat* data that show a dependence of the drizzle occurrence on both macrophysical (W_c) and microphysical ($r_{e,3.7}$) parameters. The logarithmic scale on the ordinate highlights a qualitative tendency for the fractional differences in W_p to decrease with W_c. This inference is primarily exemplified below cloud water paths of 100 g m^{-2} and effective radii of less than 10 μm, which is a subset of clouds that contains most of the nonprecipitating and weakly drizzling clouds. Other areas of the parameter space display little tendency with W_c in the fractional sensitivity of W_p to r_e.

The sensitivity at low W_c is most likely indicative of the efficiency of the autoconversion process, whereas at higher cloud water paths the sensitivity is most likely more representative of the accretion process. The dominance of the autoconversion process at low cloud water path and the accretion process at higher cloud water path is elucidated through simple heuristic models in much greater detail by Wood et al. (2009), who suggest that the fractional sensitivity of precipitation to microphysical perturbations decreases with W_c. That result conflicts with the concept of precipitation susceptibility presented by Sorooshian et al. (2009), who argue that precipitation is most susceptible to microphysical influence at moderate liquid water paths whereas it is moisture limited and thus insensitive to microphysics at low values of cloud water path. The limited qualitative analysis presented here would seem to support the notion that the precipitation sensitivity decreases with cloud

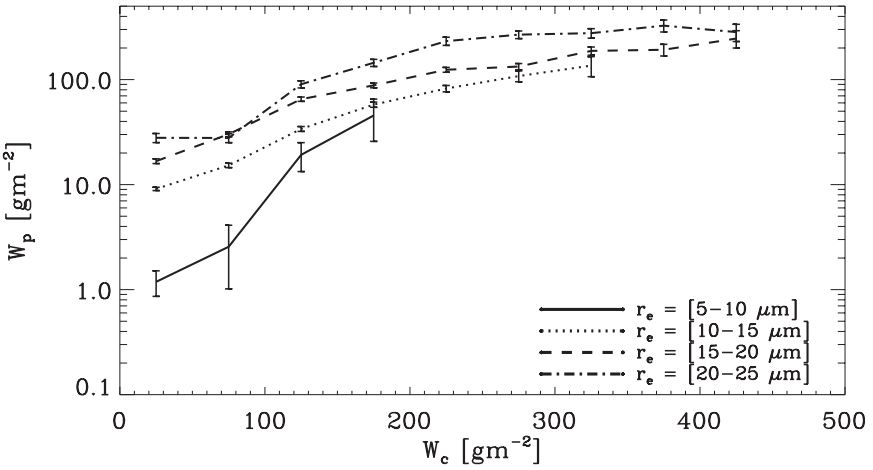

FIG. 8. The mean W_p as a function of W_c for four $r_{e,3.7}$ bins assuming a drizzle distribution. Similar results are found using the Marshall–Palmer distribution. The curves are not plotted where data sampling (n_{samples}) is less than 30 points. The error bars show the standard errors SE [$=\sigma/(n_{\text{samples}})^{1/2}$].

water path as suggested by Wood et al. (2009), although we note that these results are by no means conclusive.

The method outlined in Eqs. (9) and (10) explicitly includes a contribution to the observed optical depth from precipitation water; therefore, the results can provide some insight into the extent to which precipitation affects the observed MODIS optical depths. Figure 9 shows the median percentage of the optical depth that is due to precipitation as a function of the total observed optical depth. The influence of the precipitation optical depth is observed to increase as a function of the optical depth itself, which is consistent with the increasing values of W_p with W_c shown in Fig. 6. The result is very sensitive to the precipitation DSD, with the Marshall–Palmer model predicting precipitation optical depth influence on the order of 1% and the drizzle distribution with its smaller drop sizes predicting a median effect on the order of 5% with values that exceed 10% occasionally occurring. This result is important because it provides a rough estimate of the magnitude of the bias one might incur by associating all of the observed optical depth to cloud water when estimating W_c from visible and near-infrared observations.

5. Summary

Estimates are made of the mean relationship between the cloud water path and the precipitation water path in shallow marine clouds in the low latitudes. This is the first large-scale observational estimate of this relationship known to the authors and could provide some bounds on the assumptions that are imposed a priori in remote sensing retrievals of precipitation rate such as that used by Haynes et al. (2009) or passive microwave approaches (Kummerow et al. 2001; Hilburn and Wentz 2008). The analysis relies on the relative insensitivity of the MODIS observations to the presence of precipitation in combination with a novel approach for deducing the path-integrated attenuation using interpolation of the along-track surface reflectivity from the *CloudSat* CPR. By utilizing the relative insensitivity of the MODIS observations to precipitation and the large sensitivity of the

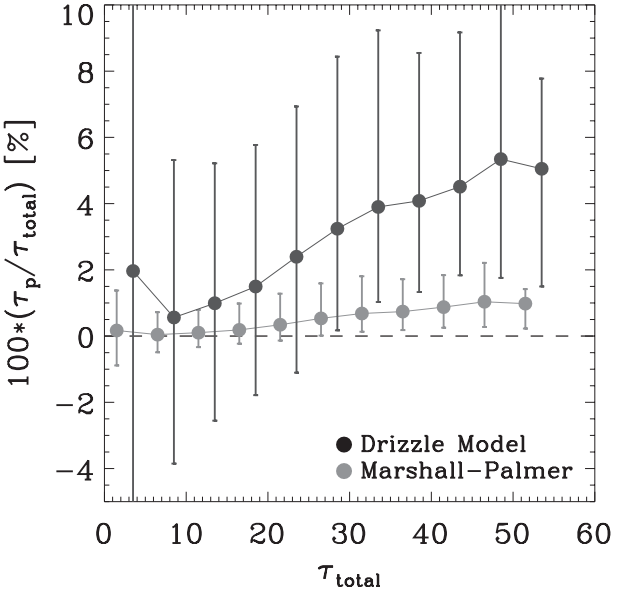

FIG. 9. The median percentage of the optical depth τ_p that is due to precipitation water, as a function of the observed optical depth τ_{total} for all pixels (nonprecipitating and precipitating). The error bars show the range encompassing 75% of the data.

PIA to the presence of precipitation, the cloud water path and the precipitation water path are deduced simultaneously.

The mean precipitation water path is shown to increase with increasing cloud water, consistent with a description of clouds in which the production of precipitation water is largely governed by the cloud water content. However, an additional dependence of the precipitation water path on the cloud effective radius is shown. The absolute magnitude of the radius dependence increases with cloud water path whereas the fractional sensitivity is largest at low values of water path, providing qualitative support of the idea that the fractional sensitivity of precipitation to cloud droplet size decreases with cloud water path.

The *CloudSat* attenuation observations are used to evaluate several estimates of the cloud water path from the MODIS instrument for nonprecipitating clouds. It was found that using the effective radius derived from the 3.7-μm channel and the assumption of an adiabatically stratified cloud minimizes the bias between the *CloudSat* attenuation and the MODIS cloud water path. Furthermore, distribution functions of effective radius derived from the MODIS 3.7- and 2.1-μm channels are presented. In an average sense, $r_{e,3.7}$ slightly overestimates $r_{e,2.1}$ when $r_{e,2.1}$ is less than 10 μm, indicating a modest tendency toward adiabadicity. The sign of this relationship reverses beyond 10 μm, suggesting the initiation of the coalescence process or potential dilution at cloud top. It is observed that the distribution of $r_{e,2.1}$ has a tail that extends beyond 30 μm, which is well beyond the size of a representative cloud droplet radius. Taken together, the above results suggest the use of $r_{e,3.7}$ when a radius associated with the cloud droplet distribution is desired. In addition, the existence of a tail of the $r_{e,2.1}$ distribution beyond 30 μm suggests that termination of the reported r_e at this arbitrary threshold is inappropriate and may result in the loss of some information regarding identification of drizzle and rain. The results suggest that the use of either an effective radius threshold or the sign of the difference of $r_{e,2.1}$ and $r_{e,3.7}$ by themselves are imprecise predictors of the presence of precipitation.

Some caveats that deserve future exploration are mentioned. A key assumption in the method presented here is that the MODIS $r_{e,3.7}$ is unaffected by the presence of precipitation. The validity of this assumption is only cursorily explored in this work and deserves a thorough exploration elsewhere. In particular, a detailed modeling study of the effects of drizzle and rain on visible/near-infrared-based estimates of cloud water path and effective radius is needed. In addition, data from several recent field campaign [i.e., the Variability Of The American Monsoon Systems (VAMOS) Ocean–Cloud–Atmosphere–Land Study (VOCALS) and the Rain In Cumulus Over Ocean (RICO)] could be exploited to shed light on this issue. One limitation of the method is the reliance on the interpolation-based method to deduce the radar-path-integrated attenuation, and future work will focus on reducing the bias in the climatological-database method for deducing the path-integrated attenuation to expand the applicability of this work. Furthermore, we have shown that the derivation of the precipitation water path is highly sensitive to the shape of the drop size distribution. Because of this sensitivity, only broad constraints are placed on the precipitation water path in this study. Substantial additional research, possibly employing aircraft data from field campaigns, is needed to characterize better the global statistics of the DSDs encountered in the full range of shallow precipitating clouds examined in this work.

Acknowledgments. This research was supported under the NASA Earth and Space Science Fellowship (NESSF) Program, Grant NNX07AO24H, and NASA Grants NNX07AR97G and NAS5-99237. The data used were obtained from the *CloudSat* Data Processing Center (DPC). The methods and the presentation benefited substantially from the thoughtful critiques of three anonymous reviewers.

REFERENCES

Ackerman, S. A., K. I. Strabala, W. P. Menzel, R. A. Frey, C. C. Moeller, and L. E. Gumley, 1998: Discriminating clear sky from clouds with MODIS. *J. Geophys. Res.,* **103,** 32 141–32 157.

Albrecht, B. A., 1989: Aerosols, cloud microphysics, and fractional cloudiness. *Science,* **245,** 1227–1230.

——, C. W. Fairall, D. W. Thomson, A. B. White, J. B. Snider, and W. H. Schubert, 1990: Surface-based remote sensing of the observed and the adiabatic liquid water content of stratocumulus clouds. *Geophys. Res. Lett.,* **17,** 89–92.

Battaglia, A., and C. Simmer, 2008: How does multiple scattering affect the spaceborne W-band radar measurements at ranges close to and crossing the surface range? *IEEE Trans. Geosci. Remote Sens.,* **46,** 1644–1651.

——, J. M. Haynes, T. L'Ecuyer, and C. Simmer, 2008: Identifying multiple-scattering-affected profiles in *CloudSat* observations over the oceans. *J. Geophys. Res.,* **113,** D00A17, doi:10.1029/2008JD009960.

Bennartz, R., 2007: Global assessment of marine boundary layer cloud droplet number concentration from satellite. *J. Geophys. Res.,* **112,** D02201, doi:10.1029/2006JD007547.

——, P. Watts, J. F. Meirink, and R. Roebeling, 2010: Rain water path in warm clouds derived from combined visible/near-infrared and microwave satellite observations. *J. Geophys. Res.,* **115,** D19120, doi:10.1029/2009JD013679.

Berg, W., T. L'Ecuyer, and J. M. Haynes, 2010: The distribution of rainfall over oceans from spaceborne radars. *J. Appl. Meteor. Climatol.,* **49,** 535–543.

Bony, S., and J.-L. Dufresne, 2005: Marine boundary layer clouds at the heart of tropical cloud feedback uncertainties in climate models. *Geophys. Res. Lett.,* **32,** L20806, doi:10.1029/2005GL023851.

Brenguier, J.-L., H. Pawlowska, and L. Schüller, 2003: Cloud microphysical and radiative properties for parameterization and satellite monitoring of the indirect effect of aerosol on climate. *J. Geophys. Res.,* **108,** 8632, doi:10.1029/2002JD002682.

Bretherton, C., M. Widmann, V. P. Dymnikov, J. M. Wallace, and I. Bladé, 1999: The effective number of spatial degrees of freedom of a time varying field. *J. Climate,* **12,** 1990–2009.

Chang, F.-L., and Z. Li, 2002: Estimating the vertical variation of cloud droplet effective radius using multispectral near-infrared satellite measurements. *J. Geophys. Res.,* **107,** 4257, doi:10.1029/2001JD000766.

Comstock, K. K., R. Wood, S. E. Yuter, and C. Bretherton, 2004: Reflectivity and rain rate in and below drizzling stratocumulus. *Quart. J. Roy. Meteor. Soc.,* **130,** 2891–2919, doi:10.1256/qj.03.187.

——, C. S. Bretherton, and S. E. Yuter, 2005: Mesoscale variability and drizzle in southeast Pacific stratocumulus. *J. Atmos. Sci.,* **62,** 3792–3807.

Dufresne, J.-L., and S. Bony, 2008: An assessment of the primary sources of spread of global warming estimates from coupled ocean–atmosphere models. *J. Climate,* **21,** 5135–5144.

Eyre, J. R., 1990: The information content of data from satellite sounding systems: A simulation study. *Quart. J. Roy. Meteor. Soc.,* **116,** 401–434.

——, G. A. Kelly, A. P. McNally, E. Anderson, and A. Persson, 1993: Assimilation of TOVS radiance information through one-dimensional variational analysis. *Quart. J. Roy. Meteor. Soc.,* **119,** 1427–1463.

Frisch, A. S., C. W. Fairall, and J. B. Snider, 1995: Measurement of stratus cloud and drizzle parameters in ASTEX with a K_α-band Doppler radar and a microwave radiometer. *J. Atmos. Sci.,* **52,** 2788–2799.

Greenwald, T. J., 2009: A 2 year comparison of AMSR-E and MODIS cloud liquid water path observations. *Geophys. Res. Lett.,* **36,** L20805, doi:10.1029/2009GL040394.

Haynes, J. M., and G. L. Stephens, 2007: Tropical oceanic cloudiness and the incidence of precipitation: Early results from *CloudSat*. *Geophys. Res. Lett.,* **34,** L09811, doi:10.1029/2007GL029335.

——, T. S. L'Ecuyer, G. L. Stephens, S. D. Miller, C. Mitrescu, N. B. Wood, and S. Tanelli, 2009: Rainfall retrieval over the ocean with spaceborne W-band radar. *J. Geophys. Res.,* **114,** D00A22, doi:10.1029/2008JD009973.

Hilburn, K. A., and F. J. Wentz, 2008: Intercalibrated passive microwave rain products from the unified microwave ocean retrieval algorithm (UMORA). *J. Appl. Meteor. Climatol.,* **47,** 778–794.

Iguchi, T., T. Kozu, R. Meneghini, J. Awaka, and K. Okamoto, 2000: Rain-profiling algorithm for the TRMM precipitation radar. *J. Appl. Meteor.,* **39,** 2038–2052.

Kubar, T. L., D. L. Hartmann, and R. Wood, 2009: Understanding the importance of microphysics and macrophysics for warm rain in marine low clouds. Part II: Heuristic models of rain formation. *J. Atmos. Sci.,* **66,** 2973–2990.

Kummerow, C., W. Barnes, T. Kozu, J. Shiue, and J. Simpson, 1998: The Tropical Rainfall Measuring Mission (TRMM) sensor package. *J. Atmos. Oceanic Technol.,* **15,** 808–816.

——, and Coauthors, 2001: The evolution of the Goddard Profiling algorithm (GPROF) for rainfall estimation from passive microwave sensors. *J. Appl. Meteor.,* **40,** 1801–1820.

Lebsock, M. D., G. L. Stephens, and C. Kummerow, 2008: Multisensor satellite observations of aerosol effects on warm clouds. *J. Geophys. Res.,* **113,** D15205, doi:10.1029/2008JD009876.

L'Ecuyer, T. S., and G. L. Stephens, 2002: An estimation-based precipitation retrieval algorithm for attenuating radars. *J. Appl. Meteor.,* **41,** 272–285, doi:10.1175/1520-0450.

——, and J. H. Jiang, 2010: Touring the atmosphere aboard the A-Train. *Phys. Today,* **63,** 36–41.

——, W. Berg, J. Haynes, M. Lebsock, and T. Takemura, 2009: Global observations of aerosol impacts on precipitation occurrence in warm maritime clouds. *J. Geophys. Res.,* **114,** D09211, doi:10.1029/2008JD011273.

Leon, D. C., Z. Wang, and D. Liu, 2008: Climatology of drizzle in marine boundary layer clouds based on 1 year of data from *CloudSat* and *Cloud-Aerosol Lidar and Infrared Pathfinder Satellite Observations* (*CALIPSO*). *J. Geophys. Res.,* **113,** D00A14, doi:10.1029/2008JD009835.

Lhermitte, R., 1990: Attenuation and scattering of millimeter wavelength radiation by clouds and precipitation. *J. Atmos. Oceanic Technol.,* **7,** 464–479.

Marshall, J. S., and W. McK. Palmer, 1948: The distribution of raindrops with size. *J. Atmos. Sci.,* **5,** 165–166.

Masunaga, H., T. Y. Nakajima, T. Nakajima, M. Kachi, R. Oki, and S. Kuroda, 2002a: Physical properties of maritime low clouds as retrieved by combined use of Tropical Rainfall Measurement Mission Microwave Imager and Visible/Infrared Scanner: Algorithm. *J. Geophys. Res.,* **107,** 4083, doi:10.1029/2001JD000743.

——, ——, ——, ——, and K. Suzuki, 2002b: Physical properties of maritime low clouds as retrieved by combined use of Tropical Rainfall Measuring Mission (TRMM) Microwave Imager and Visible/Infrared Scanner 2. Climatology of warm clouds and rain. *J. Geophys. Res.,* **107,** 4367, doi:10.1029/2001JD001269.

Matrosov, S. Y., T. Uttal, and D. A. Hazen, 2004: Evaluation of radar reflectivity–based estimates of water content in stratiform marine clouds. *J. Appl. Meteor.,* **43,** 405–419.

Mitrescu, C., T. L'Ecuyer, J. Haynes, S. Miller, and J. Turk, 2010: *CloudSat* Precipitation Profiling algorithm—Model description. *J. Appl. Meteor. Climatol.,* **49,** 991–1003.

Nakajima, T. Y., K. Suzuki, and G. L. Stephens, 2010: Droplet growth in warm water clouds observed by the A-Train. Part I: Sensitivity analysis of the MODIS-derived cloud droplet sizes. *J. Atmos. Sci.,* **67,** 1884–1896.

Paluch, I. R., and D. H. Lenschow, 1991: Stratiform cloud formation in the marine boundary layer. *J. Atmos. Sci.,* **48,** 2141–2158.

Pawlowska, H., and J.-L. Brenguier, 2003: An observational study of drizzle formation in stratocumulus clouds for general circulation model (GCM) parameterizations. *J. Geophys. Res.,* **108,** 8630, doi:10.1029/2002JD002679.

Platnick, S., 2000: Vertical photon transport in cloud remote sensing problems. *J. Geophys. Res.,* **105,** 22 919–22 935.

——, M. D. King, S. A. Ackerman, W. P. Menzel, B. A. Baum, J. C. Riedi, and R. A. Frey, 2003: The MODIS cloud products: Algorithms and examples from *Terra*. *IEEE Trans. Geosci. Remote Sens.,* **41,** 459–473.

Rapp, A. D., G. Elsaesser, and C. Kummerow, 2009: A combined multisensor optimal estimation retrieval algorithm for oceanic warm rain clouds. *J. Appl. Meteor. Climatol.,* **48,** 2242–2256.

Rauber, R. M., and Coauthors, 2007: Rain in Shallow Cumulus over the Ocean: The RICO campaign. *Bull. Amer. Meteor. Soc.,* **88,** 1912–1928.

Shao, H., and G. Liu, 2004: Detecting drizzle in marine warm clouds using combined visible, infrared, and microwave satellite data. *J. Geophys. Res.,* **109,** D07205, doi:10.1029/2003JD004286.

Sorooshian, A., G. Feingold, M. D. Lebsock, H. Jiang, and G. L. Stephens, 2009: On the precipitation susceptibility of clouds to aerosol perturbations. *Geophys. Res. Lett.,* **36,** L13803, doi:10.1029/2009GL038993.

Stephens, G. L., 1978: Radiation profiles in extended water clouds. Part II: Parameterization schemes. *J. Atmos. Sci.,* **35,** 2123–2132.

——, 2005: Cloud feedbacks in the climate system: A critical review. *J. Climate,* **18,** 237–273.

——, and Coauthors, 2002: The *CloudSat* mission and the A-train. *Bull. Amer. Meteor. Soc.,* **83,** 1771–1790.

——, and Coauthors, 2008: *CloudSat* mission: Performance and early science after the first year of operation. *J. Geophys. Res.,* **113,** D00A18, doi:10.1029/2008JD009982.

Stevens, B., W. R. Cotton, G. Feingold, and C.-H. Moeng, 1998: Large-eddy simulations of strongly precipitating, shallow, stratocumulus-topped boundary layers. *J. Atmos. Sci.,* **55,** 3616–3638.

——, G. Vali, K. Comstock, R. Wood, M. van Zanten, P. H. Austin, C. S. Bretherton, and D. H. Lenschow, 2005: Pockets of open cells and drizzle in marine stratocumulus. *Bull. Amer. Meteor. Soc.,* **86,** 51–57.

Szczodrak, M., P. H. Austin, and P. B. Krummel, 2001: Variability of optical depth and effective radius in marine stratocumulus clouds. *J. Atmos. Sci.,* **58,** 2912–2926.

vanZanten, M. C., and B. Stevens, 2005: Observations of the structure of heavily precipitating marine stratocumulus. *J. Atmos. Sci.,* **62,** 4327–4342.

Wang, H., and G. Feingold, 2009: Modeling mesoscale cellular structures and drizzle in marine stratocumulus: Impact of drizzle on the formation and evolution of open cells. *J. Atmos. Sci.,* **66,** 3237–3256.

Warner, J., 1970: On steady-state one-dimensional models of cumulus convection. *J. Atmos. Sci.,* **27,** 1035–1040.

Webb, M. J., and Coauthors, 2006: On the contribution of local feedback mechanisms to the range of climate sensitivity in two GCM ensembles. *Climate Dyn.,* **27,** 17–38, doi:10.1007/s00382-006-0111-2.

Winker, D. M., W. H. Hunt, and M. J. McGill, 2007: Initial performance assessment of CALIOP. *Geophys. Res. Lett.,* **34,** L19803, doi:10.1029/2007GL030135.

Wood, R., 2005a: Drizzle in stratiform boundary layer clouds. Part I: Vertical and horizontal structure. *J. Atmos. Sci.,* **62,** 3011–3033.

——, 2005b: Drizzle in stratiform boundary layer clouds. Part II: Microphysical aspects. *J. Atmos. Sci.,* **62,** 3034–3050.

——, K. K. Comstock, C. S. Bretherton, C. Cornish, J. Tomlinson, D. R. Collins, and C. Fairall, 2008: Open cellular structure in marine stratocumulus sheets. *J. Geophys. Res.,* **113,** D12207, doi:10.1029/2007JD009371.

——, T. L. Kubar, and D. L. Hartmann, 2009: Understanding the importance of microphysics and macrophysics for warm rain in marine low clouds. Part II: Heuristic models of rain formation. *J. Atmos. Sci.,* **66,** 2953–2972.